

# Heterochromatic Nonlinear Optical Responses in Upconversion Nanoparticles for Super-Resolution Nanoscopy

Chaohao Chen, Baolei Liu, Yongtao Liu, Jiayan Liao, Xuchen Shan, Fan Wang,\*  
and Dayong Jin\*

Point spread function (PSF) engineering by an emitter's response can code higher-spatial-frequency information of an image for microscopy to achieve super-resolution. However, complexed excitation optics or repetitive scans are needed, which explains the issues of low speed, poor stability, and operational complexity associated with the current laser scanning microscopy approaches. Here, the diverse emission responses of upconversion nanoparticles (UCNPs) are reported for super-resolution nanoscopy to improve the imaging quality and speed. The method only needs a doughnut-shaped scanning excitation beam at an appropriate power density. By collecting the four-photon emission of single UCNPs, the high-frequency information of a super-resolution image can be resolved through the doughnut-emission PSF. Meanwhile, the two-photon state of the same nanoparticle is oversaturated, so that the complementary lower-frequency information of the super-resolution image can be simultaneously collected by the Gaussian-like emission PSF. This leads to a method of Fourier-domain heterochromatic fusion, which allows the extended capability of the engineered PSFs to cover both low- and high-frequency information to yield optimized image quality. This approach achieves a spatial resolution of 40 nm, 1/24th of the excitation wavelength. This work suggests a new scope for developing nonlinear multi-color emitting probes in super-resolution nanoscopy.

become the essential scheme for super-resolution imaging. Approaches based on the point-scanning nonlinear illumination<sup>[5]</sup> can obtain extraordinary high efficacy in resolution enhancement. Stimulated emission depletion (STED) microscopy is a prominent example of point spread functions (PSF) engineering by generating doughnut-shaped beam<sup>[6]</sup> to resolve higher spatial frequencies in the doughnut spot than a diffraction-limited Gaussian PSF.<sup>[7]</sup> By using exclusively doughnut-shaped excitation spots to saturate fluorescence, new modalities<sup>[8–11]</sup> have been demonstrated to extract the extraordinary information at the higher spatial frequency for resolution enhancement. In the latest development, using upconversion nanoparticles (UCNPs),<sup>[12]</sup> single scan using two synchronized laser beams has resulted in a fluorescence emission difference microscopy approach that uses the two-color PSF engineering. Explorations of the nonlinear properties of fluorescent probes, either inducing binary stochastic methods,<sup>[13,14]</sup> quantum coherent control,<sup>[15]</sup> or under saturated conditions,<sup>[16–19]</sup> have resulted in the new approaches of stimulated emission,<sup>[6,20]</sup> ground state depletion,<sup>[9]</sup> absorption,<sup>[21,22]</sup> or fluorescence photoswitching.<sup>[23]</sup> Nevertheless, as a prerequisite to extract the broader coverage of spatial information to enhance the quality of super-resolution images, these advances still require specialized optics to meet the particular excitation conditions to produce images with multiplexed PSF. As a consequence, the complexed optics and efforts in maintaining the proper alignments and system stabilities are the critical limiting factors for point-scanning super-resolution microscopes to be widely used in material science and biology labs.

UCNPs have attracted considerable attentions as a new type of multiphoton probes doped with high-density emitters in small volumes of optically inert nanocrystal host.<sup>[24–27]</sup> Each UCNP contains thousands of co-doped lanthanide ions that form a network of photon sensitizers (ytterbium ions, Yb<sup>3+</sup>) and activators (thulium ions, Tm<sup>3+</sup>), which underpins the unique optical property of converting near-infrared (NIR) to shorter wavelength NIR, visible, and ultraviolet emissions.<sup>[28–31]</sup> More interestingly, the doped lanthanide ions have multiple intermediate energy states, and those long-lived states work like a “ladder” to support electron transfers between different

## 1. Introduction

To overcome the optical diffraction limit, techniques using patterned light excitation, such as fringes<sup>[1,2]</sup> and speckles<sup>[3,4]</sup>

Dr. C. Chen, B. Liu, Dr. Y. Liu, Dr. J. Liao, X. Shan, Dr. F. Wang,  
Prof. D. Jin  
Institute for Biomedical Materials & Devices (IBMD)  
Faculty of Science  
University of Technology Sydney  
Sydney, NSW 2007, Australia  
E-mail: fan.wang@uts.edu.au; dayong.jin@uts.edu.au

Dr. F. Wang  
School of Electrical and Data Engineering  
Faculty of Engineering and Information Technology  
University of Technology Sydney  
Sydney, NSW 2007, Australia

Prof. D. Jin  
UTS-SUStech Joint Research Centre for Biomedical Materials & Devices  
Department of Biomedical Engineering  
Southern University of Science and Technology  
Shenzhen 518055, China

 The ORCID identification number(s) for the author(s) of this article can be found under <https://doi.org/10.1002/adma.202008847>.

DOI: 10.1002/adma.202008847

states. This not only leads to the multicolor emissions from a single UCNP but also provides a diverse range of multiphoton responses of each multiphoton emission from each intermediate excited state. Recent studies have indicated that UCNPs with unique nonlinear optical response and saturation properties can be developed as novel fluorescent probes,<sup>[32–37]</sup> especially for the sub-diffraction imaging technologies.<sup>[38–41]</sup> Most recently, the dual NIR (980 nm excitation and 800 nm emission) working wavelength in UCNPs shows its utility in deep tissue super-resolution imaging,<sup>[18,42]</sup> but the doughnut-shaped PSF induces artifacts during the deconvolution process, as a certain band of frequency has been lost in the Fourier domain,<sup>[43,44]</sup> affecting the imaging quality. Ideally, simultaneously obtaining diverse PSFs using a simple setup, maximizing spatial information in the Fourier domain, would enhance the spatial resolution and overall imaging quality.

Here, we investigate the heterochromatic nonlinear responses and saturated fluorescence emissions of UCNPs. By using a single doughnut-shaped beam point-scanning illumination, we report a new strategy by exploring the opportunities in multicolor emission PSF engineering in the image's Fourier domain. We develop a multicolor Fourier domain fusion algorithm to enlarge the frequency shifting coverage of the optical system, and thereby achieve the effective super-resolution PSF by fusing Fourier components from each emission bands and processing optical transfer function (OTF) that contains the optimized spatial information.

## 2. Results

We first mathematically and experimentally demonstrate the concept of heterochromatic nonlinear optical responses from a single lanthanide-doped nanoparticle. UCNPs used in this work are based on a NaYF<sub>4</sub> nanocrystal host co-doped with the high concentrations of 40% Yb<sup>3+</sup> sensitizer ions and 4% Tm<sup>3+</sup> activator ions. These particles have uniform morphologies with a size of 47 nm (see Figure 1a for the transmission electron microscopy (TEM) image). Under 980 nm excitation, the UCNPs show stable and bright emissions, e.g., 12 500 counts per 50 ms with 7.8% standard deviations (see Figure 1b for the confocal scanning image). Figure 1c and Figure S1 in the Supporting Information display the typical emission spectra of the UCNPs in NIR region and full spectrum, respectively. Benefiting from the multiple long-lived intermediate states, the sensitized photon energy can be stepwise transferred onto the scaffold energy levels of Tm<sup>3+</sup> emitters, which eventually facilitates the multiphoton upconversion emissions from the two-photon excited state (800 nm, <sup>3</sup>H<sub>4</sub> → <sup>3</sup>H<sub>6</sub>) and four-photon excited state (740 nm, <sup>1</sup>D<sub>2</sub> → <sup>3</sup>H<sub>4</sub>). The upconversion emission at 800 nm from the lower intermediate excited level has a lower saturation threshold, compared with emissions from the higher levels, as confirmed by the nonlinear fluorescence saturation curves shown in Figure 1d.

By taking advantage of the clear contrast in saturation intensity curves of upconversion emissions from the

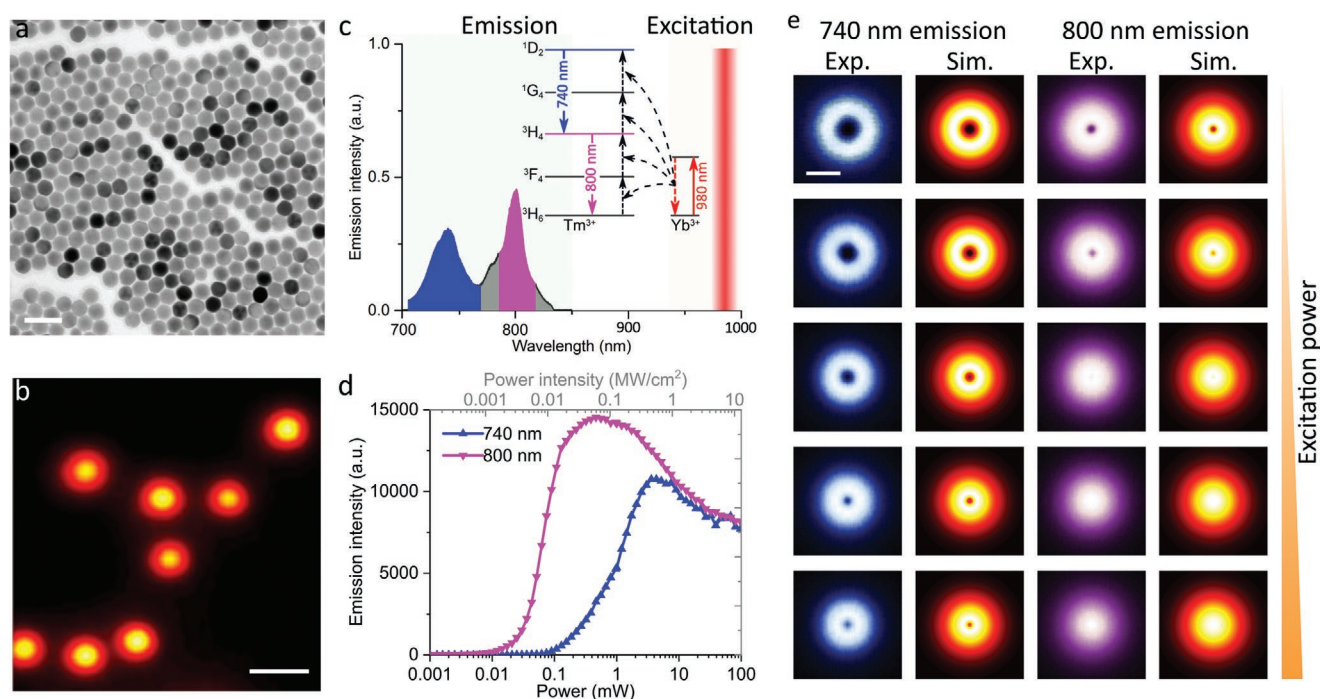


**Figure 1.** Heterochromatic emission saturation contrast in UCNPs. a) TEM image of the nanoparticles NaYF<sub>4</sub>: 40% Yb<sup>3+</sup>, 4% Tm<sup>3+</sup>. The average size is around 47 nm. b) Confocal imaging of the UCNPs under 980 nm excitation. c) The upconversion emission spectrum of a typical single nanoparticle upon 980 nm excitation laser at a power of 100 mW. Inset is a simplified energy level and upconversion process of Yb<sup>3+</sup> and Tm<sup>3+</sup> co-doped UCNPs. The multiphoton near-infrared (NIR) upconversion emissions mainly from the two-photon excited state (800 nm, <sup>3</sup>H<sub>4</sub> → <sup>3</sup>H<sub>6</sub>) and four-photon excited state (740 nm, <sup>1</sup>D<sub>2</sub> → <sup>3</sup>H<sub>4</sub>). d) The two distinct power-dependent saturation intensity curves of the 800 and 740 nm emissions. e) The experimental and simulation results of the power-dependent PSF patterns of two emission bands from a single UCNP under the 980 nm doughnut-shaped beam with excitation powers of 5, 20, 50, 100, and 150 mW. Pixel size, 10 nm. Scale bar is 100 nm in (a), 1 μm in (b), and 500 nm in (e).

multi-intermediate states,<sup>[45]</sup> we scan the sample of single UCNPs using a tightly focused doughnut illumination beam and detect their emissions from multiple emission channels, including 800 and 740 nm, as shown in Figure 1e (see the experimental setup in Figure S2, Supporting Information). We find that under the low excitation power, both channels display the doughnut-pattern PSFs. The difference in heterochromatic emission PSFs becomes significant with an increased excitation power. Because of the non-zero feature at the center dip of doughnut beam (around 1.4%, see Figure S2, Supporting Information), at an intense power, the 800 nm oversaturated emission PSF eventually becomes a “Gaussian-like PSF” with two-photon upconversion emission at center reaching the maxima (Figure 1e). This is because the increased excitation power elevates the two-photon fluorescence at the center to reach the maxima, while the fluorescence signals away from the center keep at the same values since they have been saturated. In contrast, the 740 nm emission PSF remains as a doughnut shape.

Encouraged by the attractive heterochromatic nonlinear optical responses, we propose the general concept of PSF engineering strategies in our single-doughnut-beam scanning

super-resolution microscopy (Figure 2). It takes advantage of heterochromatic saturated emission PSFs from a multi-color emitting probe. Instead of creating the contrast from dual-beam (de-) excitation patterns, the emission in different color bands can have distinct power-dependent responses to a single doughnut excitation, so that to display the different emission PSF patterns, e.g., red PSF<sub>Gau</sub> (Gaussian PSF) and green PSF<sub>Dou</sub> (doughnut PSF), as shown in Figure 2a. Due to the emission saturation effect,<sup>[22]</sup> the emission doughnut PSF contains more information at high spatial frequency. This first offers the spatial domain opportunity in PSF engineering by simply subtracting the image of PSF<sub>Dou</sub> from the one of PSF<sub>Gau</sub> with an appropriate normalizing coefficient, following  $PSF_{FED} = PSF_{Gau} - r \times PSF_{Dou}$ , so that the sub-diffraction image can be obtained by a single beam scanning super-resolution microscopy (Figure 2b and Figure S3, Supporting Information). This approach is compatible with the typical laser scanning microscope by adding a vortex phase plate to generate a doughnut excitation beam.

Nevertheless, the process of spatial domain subtraction toward super-resolution images can introduce negative PSF

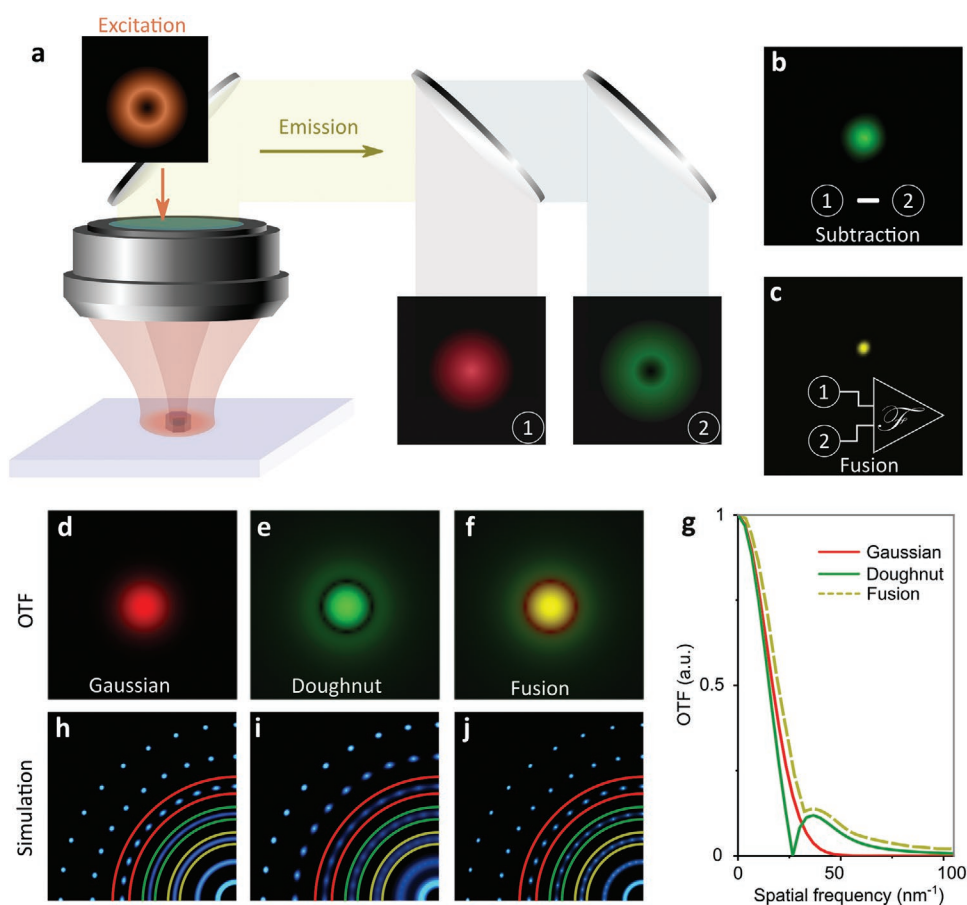


**Figure 2.** Concepts of heterochromatic PSF engineering. a) One doughnut illumination beam generates two power-dependent emission PSF patterns of Gaussian in red (1) and doughnut in green (2). b) PSF engineering by subtracting the doughnut PSF from Gaussian PSF in the spatial domain. c) PSF engineering by fusing the two PSFs in the Fourier domain. d–f) The OTFs of Gaussian PSF, doughnut PSF, and OTF fusion result of Gaussian and doughnut PSFs. The zero spatial frequency starts from the center of each image, and higher orders of frequencies increase radially. g) Normalized center cross-section profile of OTFs corresponding to (f). h–j) Simulated images of a series of dots of PSFs separated by different distances and super-resolved by Gaussian PSF (see (d)), doughnut PSF (see (e)), and synthesized PSFs (see (f)). Iterations in (h) to (j) are all 180.

components that lead to inaccurate OTF. The direct subtraction of a set of normalized data often generates areas with negative intensity values, which causes significant data loss and image distortion. Therefore, we introduce the contrast factor  $r$  to adjust the strength of the subtraction. Since the subtraction method leads to the loss in critical spatial frequencies, researchers further employ a pixel assignment<sup>[46]</sup> approach to adjust the contrast factor in each pixel, but at the expense of the overall resolution.

Alternatively, we can transfer the heterochromatic emission PSFs into the Fourier domain and achieve the super-resolution imaging with frequency shifting mechanism conceptualization. As illustrated in Figure 2c, this strategy can effectively overcome the issues of information loss and image distortion associated with the spatial domain subtraction approach, as Fourier domain OTF fusion can maximize the overall coverage of emission PSF patterns.

More specifically, by using a doughnut-shaped excitation beam, the spatial frequency components are encoded into the images by both the doughnut emission PSF and the Gaussian-like emission PSF (obtained from the oversaturated doughnut emission PSF). Benefiting from the emission saturation effect, the saturating doughnut emission PSF (Figure 2e) contains more information at a high spatial frequency than the Gaussian-like emission PSF, so that the high spatial frequency components can be captured in the extended range of the detection OTF to achieve super-resolution imaging. In the Fourier domain, the doughnut PSF has a gap in the intermediate frequency range (Figure 2e), resulting in a deficient content loss of the intermediate spatial frequency information. The Gaussian-like PSF (Figure 2d) can compensate the lost intermediate/low-frequency components. Therefore, heterochromatic OTF fusion of emission PSFs in Fourier domain takes advantage of both the doughnut PSF resolving power in providing the high-frequency contents and the compensation effect from Gaussian-like PSF that covers the medium frequency range (Figure 2f).

With more details of the fusion process described in the Supporting Information, briefly, we first perform a 2D fast Fourier transformation to convert the images that contain the doughnut PSF and the Gaussian-like PSF into Fourier domain images (Figure S4, Supporting Information). We then segment and combine the Fourier domain images into one “segmented Fourier image” by applying a Fourier binary mask, before the reconstruction by the inverse fast Fourier transformation (Figure S5, Supporting Information). Figure 2g shows the line profiles of the Gaussian-like, doughnut and Fusion OTFs, illustrating the segmenting process in 1D. The amplitude indicates the resolving power at a certain spatial frequency. The cut-off frequency ( $f_{\text{cut}}$ ) is found at the cross-point between the Gaussian-like OTF and the doughnut OTF. The segmented OTF (fusion OTF) combines the Gaussian-like OTF (spatial frequency from 0 to  $f_{\text{cut}}$ ) with the doughnut OTF (spatial frequency  $> f_{\text{cut}}$ ) toward a large amplitude envelope.

To compare the image-resolving powers of the Gaussian-like emission PSF, the doughnut emission PSF, and the fused heterochromatic PSF, we perform a numerical simulation to scan different type of beams over a series of patterns consisting of diffraction limit dots of single emitters. As shown

in Figure 2h–j and Figure S6 (Supporting Information), the dots on different circles are separated with incremental distances. For the dots on the fourth ring (in green), the distance is too close for the Gaussian-like emission PSF to resolve them (Figure 2h), while the doughnut emission PSF provides a higher resolution to solve each dot (Figure 2i). For the dots with more sparse points on the third ring (in red), the doughnut PSF fails in providing some intermediate frequency information (see Figure 2i), which resulted in a poorly resolved dots on the third circle. This Fourier domain fusion approach utilizes all the complementary frequency contents, simultaneously acquired from the single doughnut beam scanning, which can optimize the image deconvolution process in super-resolution imaging and improve the distortion effect by taking all the frequency contents. As the final detected signal is the saturated emission with enhanced contrast to the background noise, it successfully revolves the higher frequencies information that is otherwise covered by the noise in confocal scanning mode (see Figure 2j in the inner ring in yellow).

Next, we apply this Fourier domain heterochromatic fusion approach on imaging single UCNPs (Figure 3). We first acquire the standard confocal images of 800 and 455 nm emission bands by scanning a standard Gaussian excitation beam (Figure S7, Supporting Information). We then obtain the pair of contrast images at 800 and 740 nm by scanning a doughnut-beam (Figure 3a,b). Neither confocal results (Figure S7, Supporting Information) nor the oversaturated image (Figure 3a) provides sufficient resolution to distinguish single UCNPs within the diffraction limit area. In contrast, the 740 nm saturating emission doughnut PSF carries the high-frequency information from the clusters of single nanoparticles (Figure 3b). Using the approach of Fourier domain heterochromatic fusion of the image by the Gaussian-like (over saturated doughnut) 800 nm emission PSF (Figure 3a, inset OTF) and the image by the saturating doughnut 740 nm emission PSF (Figure 3b, inset OTF), as shown in Figure 3c, we demonstrate the ability in resolving the discrete nanoparticles with a discernible distance of 120 nm. Furthermore, the magnified comparison images in Figure 3d–g clearly illustrate the enhanced imaging quality achieved by our Fourier domain fusion method, compared with the image deconvoluted by Gaussian-like PSF and the one processed by subtraction. As a result of the obviously different nonlinear emission responses from the multiple intermediate excited states, the varying degrees of saturating emission PSFs provide the key for the Fourier domain heterochromatic fusion of the images simultaneously obtained from the multiple emission color bands.

As the low excitation density is essential for super-resolution nanoscopy to be used for biological applications, we further demonstrate the use of 2% Tm<sup>3+</sup> and 40% Yb<sup>3+</sup> UCNPs to reduce the excitation power requirement. According to our previous works,<sup>[18]</sup> the relatively low doping concentration of activators will facilitate UCNPs to achieve the emission saturation at low excitation power. As shown in Figure 3h,i and Figure S8 (Supporting Information), under 50 mW excitation, the 800 nm emission PSF turns into a Gaussian-like profile, while the 740 nm emission PSF remains as a doughnut shaped. Using the Fourier domain heterochromatic fusion method (Figure 3k), we can resolve the two UCNPs with a distance of

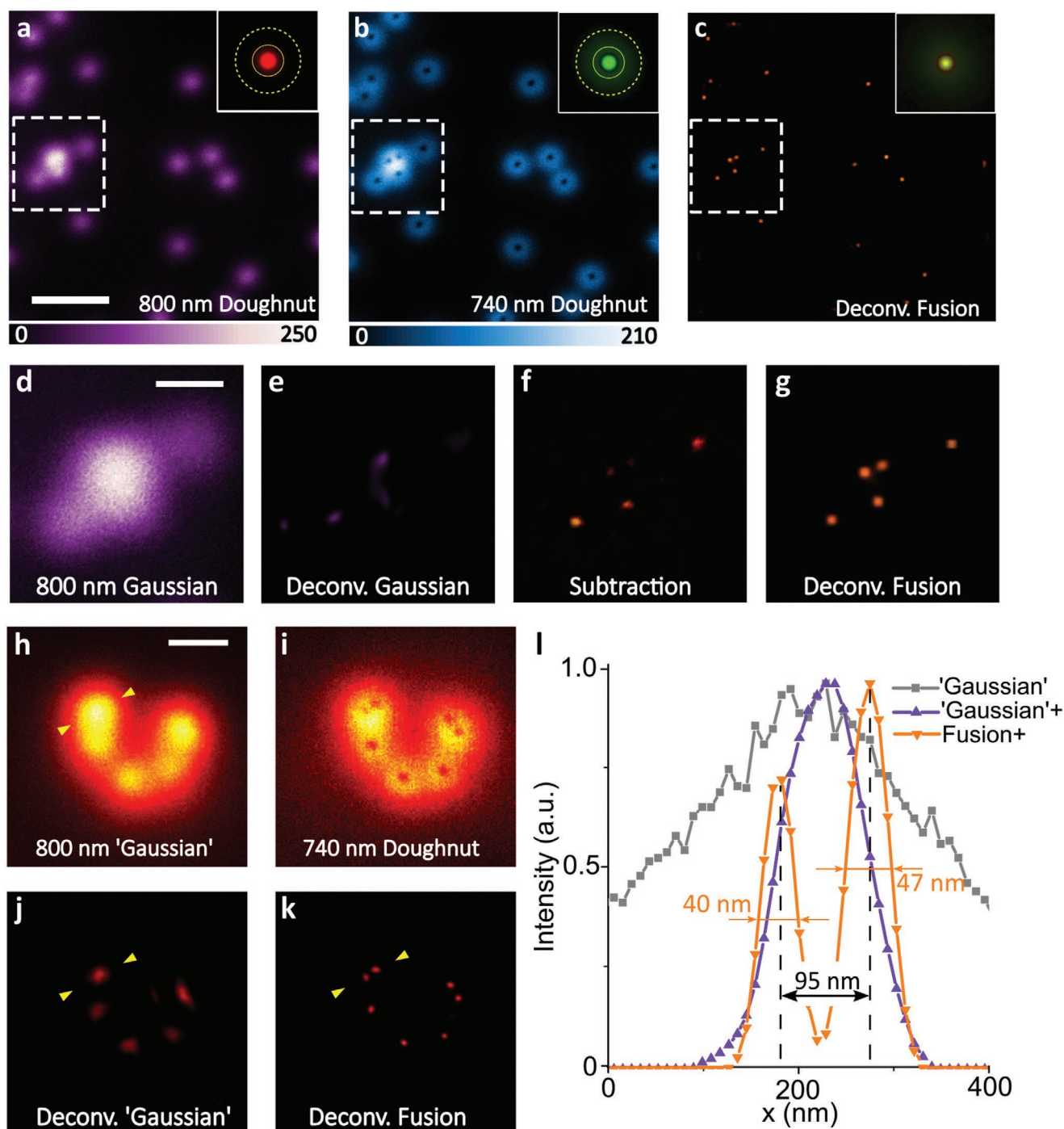


**Figure 3.** Resolving the signal UCNPs in sub-diffraction volume. a) The 800 nm emission band image of UCNPs under a 980 nm doughnut beam excitation (150 mW). With UCNPs' 800 nm emission being oversaturated, the emission PSF shows a Gaussian-like profile. Inset is the corresponding OTF. b) The 740 nm emission band image of UCNPs under the same 980 nm doughnut beam excitation, showing the doughnut emission PSF. Inset shows the corresponding OTF. c) The super-resolution imaging result by Fourier domain fusing the OTFs of (a) with (b). Inset is the fused OTF. d–g) The magnified area of interest to illustrate the comparison imaging results using the various image process algorithms, including Richardson–Lucy deconvolution with Gaussian PSF (Deconv. Gaussian) (e), subtraction of the doughnut image from the Gaussian image (Subtraction) (f), and the Fourier domain fusion (Deconv. Fusion) (g), respectively. h,i) The 800 and 740 nm emission band image under 50 mW doughnut beam, respectively. j,k) The corresponding deconvolution images in (h) and (i), respectively. l) Line profiles of two nearby UCNPs from (h) to (k). Pixel size: 10 nm. Scale bars: 1.5  $\mu\text{m}$  in (a) and (c); 500 nm in (d) to (k).

95 nm (Figure 3l). The corresponding excitation power density of  $2.75 \text{ MW cm}^{-2}$  is well below the phototoxic damage threshold for the living cells.<sup>[34,42]</sup> The line profiles of the processed image

of single nanoparticle, shown in Figure 3l, further demonstrate the quantified result of the significantly reduced full-width at half-maximum of 40 nm ( $\approx \lambda/24$ ) from 460 nm.

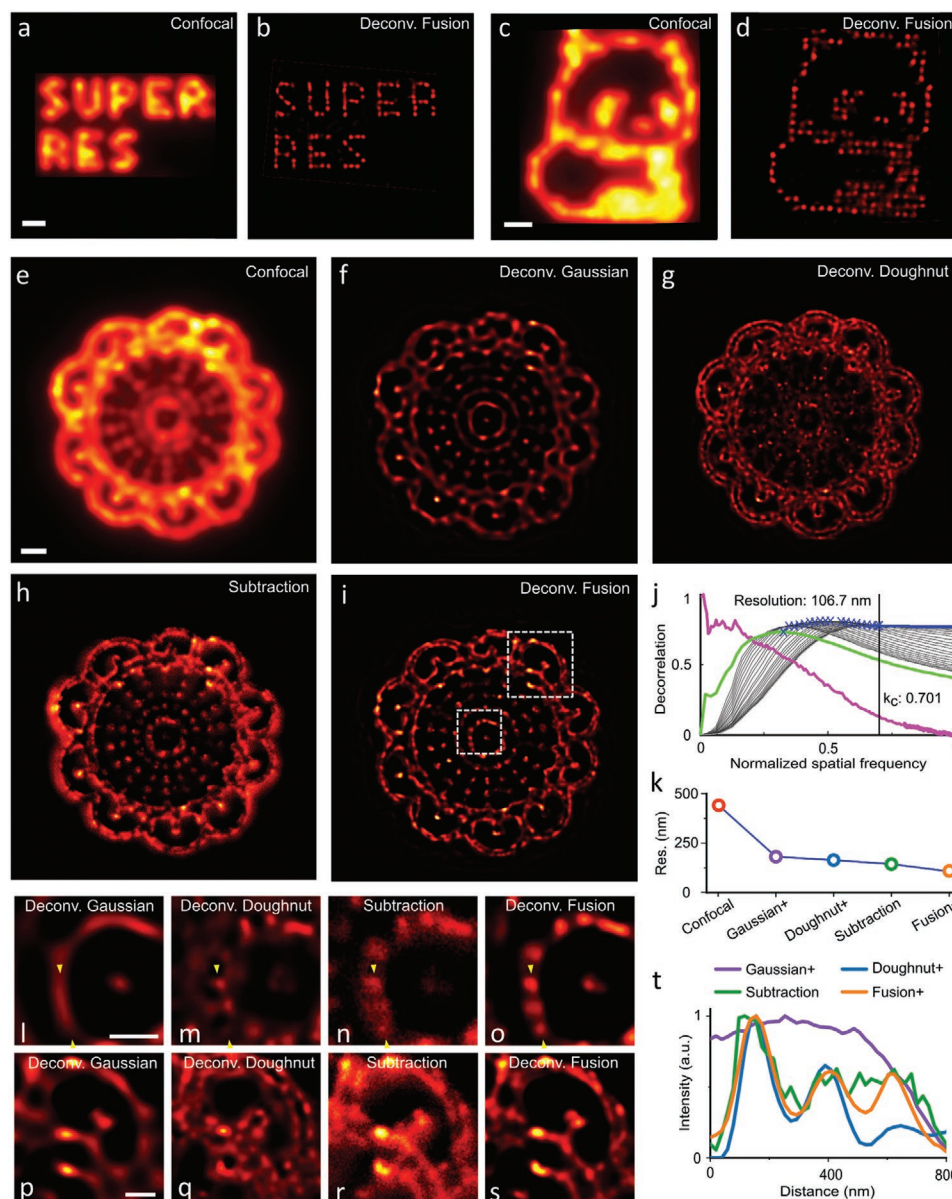


**Figure 4.** The overall enhanced image quality in super-resolution. a,b) The confocal and the Fourier domain heterochromatic fusion deconvoluted images of the “super-res” text pattern. c,d) The confocal and the Fourier domain heterochromatic fusion deconvoluted images of a panda pattern. e–i) The image results of a sunflower pattern from five processing methods: e) confocal imaging; f) Gaussian deconvolution; g) doughnut deconvolution; h) subtraction; i) Fourier domain heterochromatic fusion deconvolution. j) The decorrelation analysis for the image in (i). The resolution is  $2 \times (\text{pixel size})/k_c$ , where  $k_c$  is expressed in normalized frequencies. k) The resolution comparison for the five methods in (e) to (i). l–o, p–s) The magnified regions in (i). t) Corresponding cross-line profiles in (l) to (o). The patterns were generated by using the electron beam lithography for etching 150 nm holes on a silicon substrate. The iteration number for all the deconvolution process is 70. Pixel dwell time: 1 ms. Scale bars: 1  $\mu\text{m}$  in (a) to (i); 500 nm in (l) to (s). The panda image in Figure 4 is used with permission from Wan Yang (Weibo, <https://weibo.com/u/6021293236>).

Moreover, we apply our method of Fourier domain heterochromatic fusion to resolve UCNPs assembled into the various large-scale patterns. The scanning electron microscope images of the pattern designs are shown in Figure S9 (Supporting Information). While confocal microscopy (Figure 4a,c) cannot resolve the fine details with spacing below the diffraction limit (427 for 980 nm excitation), our Fourier-domain fusion method has successfully resolved the UCNPs image patterns (Figure 4b,d). We further quantify the resolving power

of Fourier domain fusion by comparing the image results of a sunflower pattern from confocal imaging (Figure 4e), Gaussian deconvolution (Figure 4f), doughnut deconvolution (Figure 4g), subtraction (Figure 4h), and Fourier domain fusion deconvolution methods (Figure 4i). The Fourier domain fusion approach clearly presents the best image quality. In our experiment, we apply a robust decorrelation analysis<sup>[47]</sup> to measure the averaged image resolution directly. Figure 4j shows the decorrelation analysis for the Fourier domain fusion deconvolution

images (Figure 4i), where the original image is filtered by the high-pass Gaussian filters to emphasize the specific frequency band. These filtered images are conducted with the Pearson cross-correlation (gray curves) to find the most correlated frequencies (blue cross) between each image and its normalized low-pass image. The largest number of the most correlated frequency is the cut-off frequency ( $k_c$ ), indicating the averaged resolution. Moreover, Figure 4k displays the resolutions obtained from the five methods (see decorrelation analysis in Figure S10, Supporting Information), with the Fourier domain fusion achieved the best quality in resolution (106.7 nm). Notably, the resolution by decorrelation reports the image quality, and the highest resolution is around the maximum nonzero frequency value of the image in the Fourier domain (see the magenta line). Figure 4l–o, p–s presents the detailed features of the two selected areas (Figure 4i) by the five methods. The deconvolution of confocal cannot resolve the features below the diffraction limit. The deconvoluted doughnut image shows many artifacts, due to its inherent drawback of frequency loss. Although the subtraction compensates some artifacts, it loses frequency information, e.g., the middle point cannot be presented in Figure 4h. According to the crossline profiles in Figure 4t, Fourier domain fusion shows the superior power in both resolving the fine features and managing the image artifacts. Indeed, both subtraction and deconvoluted doughnut cannot image out the third peak (at a distance of  $\approx 650$  nm).

We further simulate the imaging results for microtubules<sup>[48]</sup> to highlight the importance of compensating the missing spatial frequency regions by using the Fourier domain fusion approach (Figure S11, Supporting Information). The high image resolutions in both transverse directions are achievable for the complexed samples, as the fine structures of microtubules can be resolved using Fourier domain fusion method, as shown in Figure S11f (Supporting Information). We also apply the Fourier ring correlation<sup>[49]</sup> method to measure the resolution from the processed data (Figure S11g, Supporting Information), which presents the advances of our Fourier domain fusion approach to enhance overall image quality.

### 3. Discussion

To the best of our knowledge, this is the first work using the multicolor nonlinear emission responses and processing the simultaneously obtained PSFs in the Fourier domain to enhance the spatial resolution and overall imaging quality. It maximizes the capabilities of Fourier domain OTF fusion of multiple emission PSFs in the spectral regime to improve the entire imaging quality, which can recover the otherwise hidden spatial information during the single beam scanning and confocal detection process. Compared with the temporal domain modulation of excitation modality that requires switching illumination pattern<sup>[43]</sup> or laser mode<sup>[44]</sup> with dual excitations procedure, the single scan method is simple, fast, and stable, and can avoid the use of the additional optical components and procedures in correcting the sample drifts between multiple sequential recordings. The single-beam scanning mode using a simplified optics setup is compatible with the standard commercial or lab-based laser scanning microscopes, and therefore

may overcome the current bottleneck issue associated with the system complexity and stability.

In this work, we use a vortex phase plate to generate the doughnut excitation beam. Using a spatial light modulator with aberration correction may further reduce the required excitation power. This imaging modality presented in this work is also compatible with point-scanning-based methods, such as imaging scanning microscopy<sup>[50]</sup> or rescanning,<sup>[51]</sup> which may also help to mitigate the frequency deficiency issues. To remove the additional camera, we can further develop this technique to modulate chromatic aberrations by using multicolor phase mask.<sup>[52]</sup> Adding fast color-selection unit (e.g., acousto-optic tunable filter) in the emission collection path allows for rapid switching to collect the multiple heterochromatic images by a single detector, which will further simplify the system setup, but at the expense of the imaging speed. Moreover, the image quality could be further improved by Fourier domain fusion of the simultaneously acquired high throughput hyperspectrum PSFs (Figure S12, Supporting Information). By taking advantage of these nonlinear differential responses in the hyperspectrum domain (Figure S12d, Supporting Information), we obtain a series of emission PSFs through the parallel multicolor detection channels (Figure S12b,c, Supporting Information). Furthermore, according to the most recent discovery of a photoavalanching effect from UCNPs to provide a giant nonlinear optical response,<sup>[53]</sup> our heterochromatic function method can directly utilize such a giant nonlinear response to further improve the imaging resolution.

### 4. Conclusion

We report a single-doughnut beam scanning microscopy for super-resolution imaging. The design principle is to encode the high-frequency spatial information by PSF engineering into the multiple color channels of the image generated from the multiple excited states of UCNPs, and decode the information by engineering the Fourier domain components of the image in each of the multicolor channels according to the maximum coverage of OTF components. This approach, based on Fourier domain heterochromatic fusion method, opens a new perspective to perform super-resolution with minimum distortion and information loss, as it maximizes the coverage of all the spatial frequency details. This strategy has a great potential in improving the resolution and artificial noise management for PSF engineering-based super-resolution nanoscopy, e.g., STED microscopy,<sup>[54–57]</sup> ground states depletion microscopy,<sup>[8]</sup> structure illumination microscopy,<sup>[5]</sup> and lattice light-sheet microscopy.<sup>[58,59]</sup> Although UCNPs meet our requirement and have been successfully used in our Fourier domain heterochromatic fusion microscopy, we call for the new developments of other nonlinear optical responsive probes with multicolor emitting properties, and the combined use of existing fluorescent probes including both molecular format of organic dyes and the inorganic nanoparticles,<sup>[60]</sup> where preferably, the emission at each band should be highly dependent on the excitation power and their nonlinear optical response to excitation saturation.

## 5. Experimental Section

The experimental details are provided in the Supporting Information.

## Supporting Information

Supporting Information is available from the Wiley Online Library or from the author.

## Acknowledgements

The authors thank Joanna Szymanska and Andrew See for the pattern fabrication, performed at the NSW Node of the Australian National Fabrication Facility. The authors acknowledge the financial supports from the UTS Chancellor's Postdoctoral Research Fellowship (PRO18-6128), the Australian Research Council (ARC) DECRA fellowship (DE200100074 – F.W.), the ARC Discovery Project (DP190101058 – F.W.), National Natural Science Foundation of China (NSFC, 61729501), Major International (Regional) Joint Research Project of NSFC (51720105015), Science and Technology Innovation Commission of Shenzhen (KQTD20170810110913065), Australia China Science and Research Fund Joint Research Centre for Point-of-Care Testing (ACSRF658277, SQ2017YFGH001190), and China Scholarship Council (C.C.: no. 201607950009; B.L.: no. 201706020170; Y.L.: 201607950010; J.L.: no. 201508530231; X.S.: 201708200004).

## Conflict of Interest

The authors declare no conflict of interest.

## Data Availability Statement

The data that support the findings of this study are available from the corresponding author upon reasonable request.

## Keywords

nonlinear optical responses, PSF engineering, super-resolution imaging, upconversion nanoparticles

Received: December 31, 2020  
Revised: February 3, 2021  
Published online: April 17, 2021

- [1] A. G. York, S. H. Parekh, D. D. Nogare, R. S. Fischer, K. Temprine, M. Mione, A. B. Chitnis, C. A. Combs, H. Shroff, *Nat. Methods* **2012**, *9*, 749.
- [2] M. G. L. Gustafsson, *J. Microsc.* **2000**, *198*, 82.
- [3] E. Mudry, K. Belkebir, J. Girard, J. Savatier, E. L. Moal, C. Nicoletti, M. Allain, A. Sentenac, *Nat. Photonics* **2012**, *6*, 312.
- [4] H. Yilmaz, E. G. van Putten, J. Bertolotti, A. Lagendijk, W. L. Vos, A. P. Mosk, *Optica* **2015**, *2*, 424.
- [5] B. E. Urban, J. Yi, S. Chen, B. Dong, Y. Zhu, S. H. DeVries, V. Backman, H. F. Zhang, *Phys. Rev. E* **2015**, *91*, 042703.
- [6] T. A. Klar, S. Jakobs, M. Dyba, A. Egner, S. W. Hell, *Proc. Natl. Acad. Sci. USA* **2000**, *97*, 8206.
- [7] E. N. Ward, R. Pal, *J. Microsc.* **2017**, *266*, 221.

- [8] J. Oracz, K. Adolfsen, V. Westphal, C. Radzewicz, M. T. Borgström, S. J. Sahl, C. N. Prinz, S. W. Hell, *Nano Lett.* **2017**, *17*, 2652.
- [9] E. Rittweger, D. Wildanger, S. W. Hell, *Europhys. Lett.* **2009**, *86*, 14001.
- [10] P. Wang, M. N. Slipchenko, J. Mitchell, C. Yang, E. O. Potma, X. Xu, J.-X. Cheng, *Nat. Photonics* **2013**, *7*, 449.
- [11] B. Yang, J. B. Trebbia, R. Baby, P. Tamarat, B. Lounis, *Nat. Photonics* **2015**, *9*, 658.
- [12] B. Huang, Q. Wu, X. Peng, L. Yao, D. Peng, Q. Zhan, *Nanoscale* **2018**, *10*, 21025.
- [13] M. J. Rust, M. Bates, X. Zhuang, *Nat. Methods* **2006**, *3*, 793.
- [14] A. Beghin, A. Kechkar, C. Butler, F. Levet, M. Cabillic, O. Rossier, G. Giannone, R. Galland, D. Choquet, J.-B. Sibarita, *Nat. Methods* **2017**, *14*, 1184.
- [15] C. Liu, W. Liu, S. Wang, H. Li, Z. Lv, F. Zhang, D. Zhang, J. Teng, T. Zheng, D. Li, M. Zhang, P. Xu, Q. Gong, *Sci. Adv.* **2020**, *6*, eaaw6579.
- [16] K. Fujita, M. Kobayashi, S. Kawano, M. Yamanaka, S. Kawata, *Phys. Rev. Lett.* **2007**, *99*, 228105.
- [17] S. Chong, W. Min, X. S. Xie, *J. Phys. Chem. Lett.* **2010**, *1*, 3316.
- [18] C. Chen, F. Wang, S. Wen, Q. P. Su, M. C. L. Wu, Y. Liu, B. Wang, D. Li, X. Shan, M. Kianinia, I. Aharonovich, M. Toth, S. P. Jackson, P. Xi, D. Jin, *Nat. Commun.* **2018**, *9*, 3290.
- [19] M. Pascucci, S. Ganesan, A. Tripathi, O. Katz, V. Emiliani, M. Guillon, *Nat. Commun.* **2019**, *10*, 1327.
- [20] S. W. Hell, J. Wichmann, *Opt. Lett.* **1994**, *19*, 780.
- [21] M. G. L. Gustafsson, *Proc. Natl. Acad. Sci. USA* **2005**, *102*, 13081.
- [22] G. Zhao, M. M. Kabir, K. C. Toussaint, C. Kuang, C. Zheng, Z. Yu, X. Liu, *Optica* **2017**, *4*, 633.
- [23] T. Grotjohann, I. Testa, M. Leutenegger, H. Bock, N. T. Urban, F. Lavoie-Cardinal, K. I. Willig, C. Eggeling, S. Jakobs, S. W. Hell, *Nature* **2011**, *478*, 204.
- [24] Y. Pan, J. Yang, X. Luan, X. Liu, X. Li, J. Yang, T. Huang, L. Sun, Y. Wang, Y. Lin, Y. Song, *Sci. Adv.* **2019**, *5*, eaav7199.
- [25] A. Fernandez-Bravo, D. Wang, E. S. Barnard, A. Teitelboim, C. Tajon, J. Guan, G. C. Schatz, B. E. Cohen, E. M. Chan, P. J. Schuck, T. W. Odom, *Nat. Mater.* **2019**, *18*, 1172.
- [26] C. Clarke, D. Liu, F. Wang, Y. Liu, C. Chen, C. Ton-That, X. Xu, D. Jin, *Nanoscale* **2018**, *10*, 6270.
- [27] E. Ortiz-Rivero, K. Prorok, M. Skowicki, D. Lu, A. Bednarkiewicz, D. Jaque, P. Haro-González, *Small* **2019**, *15*, 1904154.
- [28] S. Wu, H. J. Butt, *Adv. Mater.* **2016**, *28*, 1208.
- [29] A. Lay, D. S. Wang, M. D. Wisser, R. D. Mehlenbacher, Y. Lin, M. B. Goodman, W. L. Mao, J. A. Dionne, *Nano Lett.* **2017**, *17*, 4172.
- [30] Y. Il Park, K. T. Lee, Y. D. Suh, T. Hyeon, *Chem. Soc. Rev.* **2015**, *44*, 1302.
- [31] Z. Lei, X. Ling, Q. Mei, S. Fu, J. Zhang, Y. Zhang, *Adv. Mater.* **2020**, *32*, 2070068.
- [32] C. D. S. Brites, X. Xie, M. L. Debasu, X. Qin, R. Chen, W. Huang, J. Rocha, X. Liu, L. D. Carlos, *Nat. Nanotechnol.* **2016**, *11*, 851.
- [33] S. H. Nam, Y. M. Bae, Y. Il Park, J. H. Kim, H. M. Kim, J. S. Choi, K. T. Lee, T. Hyeon, Y. D. Suh, *Angew. Chem., Int. Ed.* **2011**, *50*, 6093.
- [34] F. Wang, S. Wen, H. He, B. Wang, Z. Zhou, O. Shimoni, D. Jin, *Light: Sci. Appl.* **2018**, *7*, 18007.
- [35] X. Zeng, S. Chen, A. Weitemier, S. Han, A. Blasiak, A. Prasad, K. Zheng, Z. Yi, B. Luo, I. Yang, N. Thakor, C. Chai, K. Lim, T. J. McHugh, A. H. All, X. Liu, *Angew. Chem., Int. Ed.* **2019**, *58*, 9262.
- [36] S. Chen, A. Z. Weitemier, X. Zeng, L. He, X. Wang, Y. Tao, A. J. Y. Huang, Y. Hashimoto-dani, M. Kano, H. Iwasaki, L. K. Parajuli, S. Okabe, D. B. L. Teh, A. H. All, I. Tsutsui-Kimura, K. F. Tanaka, X. Liu, T. J. McHugh, *Science* **2018**, *359*, 679.
- [37] D. B. L. Teh, A. Bansal, C. Chai, T. B. Toh, R. A. J. Tucker, G. G. L. Gammad, Y. Yeo, Z. Lei, X. Zheng, F. Yang, J. S. Ho, N. Bolein, B. C. Wu, M. K. Gnanasammanthan, L. Hooi,

- G. S. Dawe, C. Libedinsky, W. Y. Ong, B. Halliwell, E. K. H. Chow, K. L. Lim, Y. Zhang, B. K. Kennedy, *Adv. Mater.* **2020**, *32*, 2001459.
- [38] Y. Liu, Y. Lu, X. Yang, X. Zheng, S. Wen, F. Wang, X. Vidal, J. Zhao, D. Liu, Z. Zhou, C. Ma, J. Zhou, J. A. Piper, P. Xi, D. Jin, *Nature* **2017**, *543*, 229.
- [39] A. Bednarkiewicz, E. M. Chan, A. Kotulska, L. Marciniak, K. Prorok, *Nanoscale Horiz.* **2019**, *4*, 881.
- [40] Q. Zhan, H. Liu, B. Wang, Q. Wu, R. Pu, C. Zhou, B. Huang, X. Peng, H. Ågren, S. He, *Nat. Commun.* **2017**, *8*, 1058.
- [41] B. Liu, C. Chen, X. Di, J. Liao, S. Wen, Q. P. Su, X. Shan, Z.-Q. Xu, L. A. Ju, C. Mi, F. Wang, D. Jin, *Nano Lett.* **2020**, *20*, 4775.
- [42] Y. Liu, F. Wang, H. Lu, G. Fang, S. Wen, C. Chen, X. Shan, X. Xu, L. Zhang, M. Stenzel, D. Jin, *Small* **2020**, *16*, 1905572.
- [43] G. Zhao, C. Zheng, C. Kuang, R. Zhou, M. M. Kabir, K. C. Toussaint, W. Wang, L. Xu, H. Li, P. Xiu, X. Liu, *Phys. Rev. Lett.* **2018**, *120*, 193901.
- [44] L. Thibon, M. Piché, Y. De Koninck, *Opt. Express* **2018**, *26*, 24881.
- [45] J. Liao, D. Jin, C. Chen, Y. Li, J. Zhou, *J. Phys. Chem. Lett.* **2020**, *11*, 2883.
- [46] K. Korobchevskaya, C. Peres, Z. Li, A. Antipov, C. J. R. Sheppard, A. Diaspro, P. Bianchini, *Sci. Rep.* **2016**, *6*, 25816.
- [47] A. Descloux, K. S. Grubmayer, A. Radenovic, *Nat. Methods* **2019**, *16*, 918.
- [48] Z. Zhang, 3D Nanoscale architecture of microtubule network, <https://www.nikonsmallworld.com/galleries/2017-photomicrography-competition/3d-nanoscale-architecture-of-microtubule-network> (accessed: October 2017).
- [49] R. P. J. Nieuwenhuizen, K. A. Lidke, M. Bates, D. L. Puig, D. Grünwald, S. Stallinga, B. Rieger, *Nat. Methods* **2013**, *10*, 557.
- [50] C. B. Müller, J. Enderlein, *Phys. Rev. Lett.* **2010**, *104*, 198101.
- [51] I. Gregor, M. Spiecker, R. Petrovsky, J. Großhans, R. Ros, J. Enderlein, *Nat. Methods* **2017**, *14*, 1087.
- [52] Y. Shechtman, L. E. Weiss, A. S. Backer, M. Y. Lee, W. E. Moerner, *Nat. Photonics* **2016**, *10*, 590.
- [53] C. Lee, E. Z. Xu, Y. Liu, A. Teitelboim, K. Yao, A. Fernandez-Bravo, A. M. Kotulska, S. H. Nam, Y. D. Suh, A. Bednarkiewicz, B. E. Cohen, E. M. Chan, P. J. Schuck, *Nature* **2021**, *589*, 230.
- [54] J. Hanne, H. J. Falk, F. Görlitz, P. Hoyer, J. Engelhardt, S. J. Sahl, S. W. Hell, *Nat. Commun.* **2015**, *6*, 7127.
- [55] L. Lanzanò, I. Coto Hernández, M. Castello, E. Gratton, A. Diaspro, G. Vicidomini, *Nat. Commun.* **2015**, *6*, 6701.
- [56] M. J. Sarmiento, M. Oneto, S. Pelicci, L. Pesce, L. Scipioni, M. Faretta, L. Furia, G. I. Dellino, P. G. Pelicci, P. Bianchini, A. Diaspro, L. Lanzanò, *Nat. Commun.* **2018**, *9*, 3415.
- [57] Z. Gao, J. Wang, P. Song, B. Kang, J. Xu, H. Chen, *Adv. Mater.* **2020**, *32*, 1907233.
- [58] T. Vettenburg, H. I. C. Dalgarno, J. Nylk, C. Coll-Lladó, D. E. K. Ferrier, T. Čížmár, F. J. Gunn-Moore, K. Dholakia, *Nat. Methods* **2014**, *11*, 541.
- [59] T.-L. Liu, S. Upadhyayula, D. E. Milkie, V. Singh, K. Wang, I. A. Swinburne, K. R. Mosaliganti, Z. M. Collins, T. W. Hiscock, J. Shea, A. Q. Kohrman, T. N. Medwig, D. Dambournet, R. Forster, B. Cunniff, Y. Ruan, H. Yashiro, S. Scholpp, E. M. Meyerowitz, D. Hockemeyer, D. G. Drubin, B. L. Martin, D. Q. Matus, M. Koyama, S. G. Megason, T. Kirchhausen, E. Betzig, *Science* **2018**, *360*, eaq1392.
- [60] D. Jin, P. Xi, B. Wang, L. Zhang, A. M. Van Oijen, *Nat. Methods* **2018**, *15*, 415.